Transient Absorption Measurements on Anisotropic Monolayer ReS_2

Qiannan Cui, Jiaqi He, Matthew Z. Bellus, Mirzojamshed Mirzokarimov, Tino Hofmann, Hsin-Ying Chiu, Matthew Antonik, Dawei He, Yongsheng Wang, and Hui Zhao**

***A**nisotropic optical and transport properties of monolayer ReS_2 fabricated by mechanical exfoliation are reported. Transient absorption measurements with different polarization configurations and sample orientations reveal that the absorption coefficient and transient absorption are both anisotropic, with maximal and minimal values occurring when the light polarization is parallel and perpendicular to the Re atomic chains, respectively. The maximal values are about a factor of 2.5 of the minimal values. By resolving the spatiotemporal dynamics of excitons, it is found that the diffusion coefficient of excitons moving along Re atomic chains is about 16 $cm^2\ s^{-1}$ at room temperature, which is about a factor of three larger than those moving perpendicular to that direction. An exciton lifetime of 40 ps is also extracted. These findings establish monolayer ReS_2 as an anisotropic 2D transition metal dichalcogenide.*

Q. Cui, J. He, M. Z. Bellus, Dr. H.-Y. Chiu, Dr. M. Antonik, Prof. H. Zhao
Department of Physics and Astronomy
The University of Kansas
Lawrence, KS 66045, USA
E-mail: huizhao@ku.edu

J. He, Prof. D. He, Prof. Y. Wang
Key Laboratory of Luminescence and Optical Information
Ministry of Education
Institute of Optoelectronic Technology
Beijing Jiaotong University
Beijing 100044, China
E-mail: yshwang@bjtu.edu.cn

M. Mirzokarimov, Prof. T. Hofmann
Department of Electrical and Computer Engineering
University of Nebraska-Lincoln
Lincoln, NE 68588, USA

Prof. T. Hofmann
Department of Physics
Chemistry and Biology (IFM)
Linköping, SE-581 83 Linköping, Sweden

DOI: 10.1002/smll.201501668

1. Introduction

Since 2010, there have been growing interests in developing 2D materials from layered transition metal dichalcogenides (TMDs), such as MoS_2. These 2D materials have several exotic properties, including transition to a direct band gap in monolayers,[1,2] valley-selective optical coupling,[3–5] large binding energies of excitons, trions, and biexcitons,[6–9] and strong nonlinear optical responses.[10–14] Utilizing these superior properties, significant progress has been made in developing applications of these materials in electronic[15,16] and optoelectronic[17–20] technologies. In addition, these 2D materials can be used as building blocks to fabricate new van der Waals heterostructures.[21–23]

Currently, the most extensively studied TMD members are MoS_2, WS_2, $MoSe_2$, and WSe_2. They all have 1*H* lattice structure, which dictates that their transport and linear optical properties are largely isotropic in the atomic plane. A TMD with sizable in-plane anisotropic electronic and optical properties would bring a new degree of freedom to controlling the electronic and optical responses, and allow development of TMD heterostructures with anisotropic

© 2015 Wiley-VCH Verlag GmbH & Co. KGaA, Weinheim

responses when combined with other TMDs. Here we show that monolayer ReS_2 possesses large optical and transport anisotropy.

Bulk ReS_2 is a semiconducting TMD with a room-temperature band gap of about 1.5 eV, an absorption coefficient of about 8×10^6 cm^{-1} in visible range, an exciton binding energy of about 30 meV, and room-temperature charge mobilities of about 20 cm^2 V^{-1} s^{-1}.[24–29] Unlike other TMDs, ReS_2 forms a stable distorted 1*T* structure with triclinic symmetry.[30–33] Owing to the lower lattice symmetry, bulk ReS_2 possesses in-plane anisotropic optical[28,34] and transport properties.[33] Hence, monolayer ReS_2 can potentially offer anisotropic optical and transport properties to the 2D TMD family. Very recently, monolayer ReS_2 samples have been successfully fabricated by mechanical[30,35] and liquid[36] exfoliation. It was shown that monolayers and bulk ReS_2 have similar band-structures due to the weak interlayer coupling.[30] However, the electronic and optical properties of monolayer ReS_2 have been largely unexplored.

We studied charge carrier and exciton dynamics in monolayer ReS_2 by transient absorption measurements with high time and spatial resolution. In these measurements, electron–hole pairs were excited in a monolayer ReS_2 flake by interband absorption of a pump pulse. Excitons were formed from these electron–hole pairs and were detected by measuring differential reflection of a time-delayed and spatially scanned probe pulse. We found that the magnitude of the transient absorption signal depends on the crystalline direction of the sample with respect to the polarization directions of the pump and probe pulses. Both the pump absorption and the probing efficiency were anisotropic. By performing spatially resolved measurements, we found that the exciton diffusion coefficient is also anisotropic. There results establish monolayer ReS_2 as an anisotropic 2D material.

2. Sample and Transient Absorption Scheme

The monolayer ReS_2 sample was fabricated by mechanical exfoliation. **Figure 1**a is a microscope image of the flake that contains a large and thin region. Atomic force microscope measurement indicated that the thickness of this region is about 0.8 nm, confirming its monolayer thickness (see Figure S1, Supporting Information). Figure 1b,c show the side and top views of the crystal structure of monolayer ReS_2. As discovered by density functional calculations,[30] the stable crystal structure of monolayer ReS_2 is a distorted 1*T* structure. Its unit cell, indicated by the red lines in Figure 1c, contains 4 Re and 8 S atoms. Along the **b** lattice vector direction, Re atoms form zigzag chains, as indicated by the black dashed line in Figure 1c, due to the Peierls transition. These Re atomic chains break the in-plane hexagonal symmetry, which is expected to introduce in-plane anisotropy.

Spectroscopic ellipsometry was employed to determine the complex dielectric function of the bulk ReS_2 crystal that was used to fabricate the monolayer. The results are shown in Figure 1d. The imaginary part shows a pronounced excitonic transition at 820 nm, with a width of about 17 nm. Due to the limited size of the monolayer sample, spectroscopic ellipsometry was not carried out here. Alternatively, we measured the photoluminescence of the monolayer under the excitation of a 405 nm laser beam. As shown in the inset of Figure 1d, we observed a peak centered at 800 nm with a width of about 80 nm, which is similar to a previously reported result.[30]

In our transient absorption measurements, we used a 100 fs and 730 nm pump pulse to excite the sample. The photon energy of the pump pulse is about 150 meV above the photoluminescence peak of the sample. Hence, we expect that the pump pulse excites electron–hole pairs with a large excess energy. It has been well established that the reduced dielectric screening in monolayer TMDs results in significantly enhanced exciton binding energies.[37] Since the exciton binding energy in bulk ReS_2 is about 30 meV, which is above the thermal energy at room temperature, it is reasonable to assume that in ReS_2 monolayers excitons will form from the injected electron–hole pairs, which will be stable at room temperature. The dynamics of the photocarriers and excitons were detected by measuring differential reflection of a time-delayed and spatially scanned probe pulse of 810 nm, which is near the center of the photoluminescence peak. The differential reflection, $\Delta R/R_0$, is defined as the relative change of the probe reflection caused by the pump. In all the

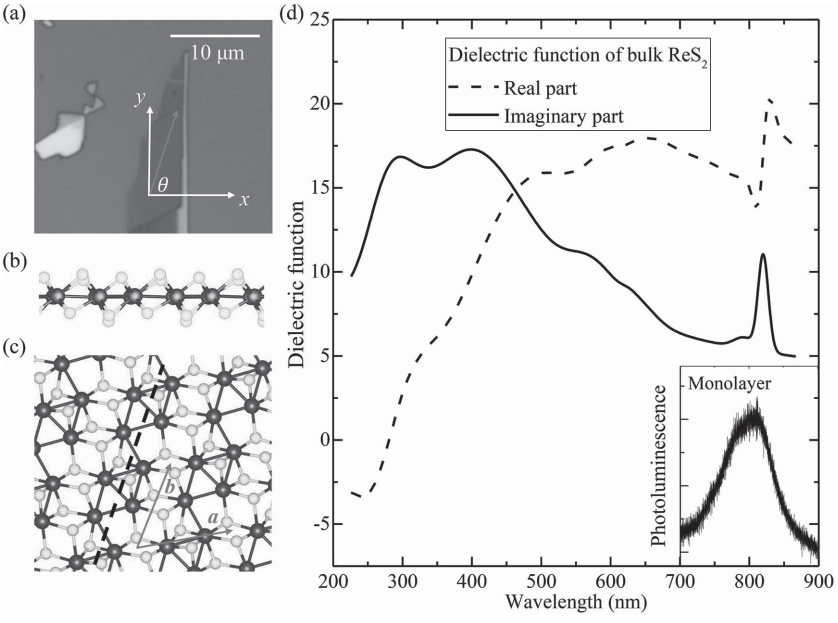

Figure 1. a) The monolayer ReS_2 sample fabricated by mechanical exfoliation. The *x*–*y* coordinates represent the laboratory frame. The orientation of the sample with respect to the laboratory frame is described by the angle *θ*. b) The side view of the crystal structure of monolayer ReS_2, which contains one Re atomic layer (dark) and two S atomic layers (light). c) The top view showing the **a** and **b** lattice vectors. Zigzag chains of Re atoms are formed along **b**. d) Complex dielectric function of the bulk ReS2 crystal obtained by spectroscopic ellipsometry. The inset shows a photoluminescence spectrum of the monolayer sample.

© 2015 Wiley-VCH Verlag GmbH & Co. KGaA, Weinheim

measurements, the pump pulse is linearly polarized along the horizontal direction in the laboratory frame, defined as x in Figure 1a. The probe polarization is either horizontal or vertical (y). We use the angle (θ) from the $+x$ direction to one of the edges of the flake, indicated as the red arrow in Figure 1a, to describe the crystalline orientation with respect to the polarizations. By mounting the sample on a rotation stage, θ can be varied with an accuracy of better than 1°.

3. Time Resolved Transient Absorption

We first present time-resolved $\Delta R/R_0$ with x-polarized pump and probe pulses, and with the sample orientation of $\theta = 0°$, as shown as the black squares in **Figure 2**a. Here the pump fluence is 25 μJ cm^{-2}. By using an absorption coefficient of 8×10^6 m^{-1} (bulk value)[24] and assuming that each pump photon absorbed generates one electron–hole pair, we estimate that an area carrier density of 5×10^{11} cm^{-2} is injected at the center of the pump spot. We found that the signal reaches a peak slightly after zero probe delay, indicating immediate response of the probe to the injected carriers. The decay of the signal can be fit by a biexponential function (red line), with two time constants of 10 ± 1 and 40 ± 2 ps, respectively. Next, we rotated the sample to $\theta = 90°$ and repeated the measurement. As shown as the blue circles in Figure 2a, the magnitude of the signal is decreased by about a factor of 7, while the bi-exponential function with the same time constants (red line) can satisfactorily describe the decay of the signal. These two measurements were repeated with a y-polarized probe. The results are shown in Figure 2b. We found that these two curves have similar magnitudes, both being smaller than $\theta = 0°$ but larger than $\theta = 90°$ in the x–x pump–probe configuration. Furthermore, the decay of both curves can also be described by the biexponential function with time constants of 10 and 40 ps (red lines). By repeating the measurements with different values of the pump fluence, we found that the dynamics are independent of the pump fluence, and the magnitude of the signal increases linearly with the fluence, as shown in Figure 2c,d for x–x and x–y configurations, respectively.

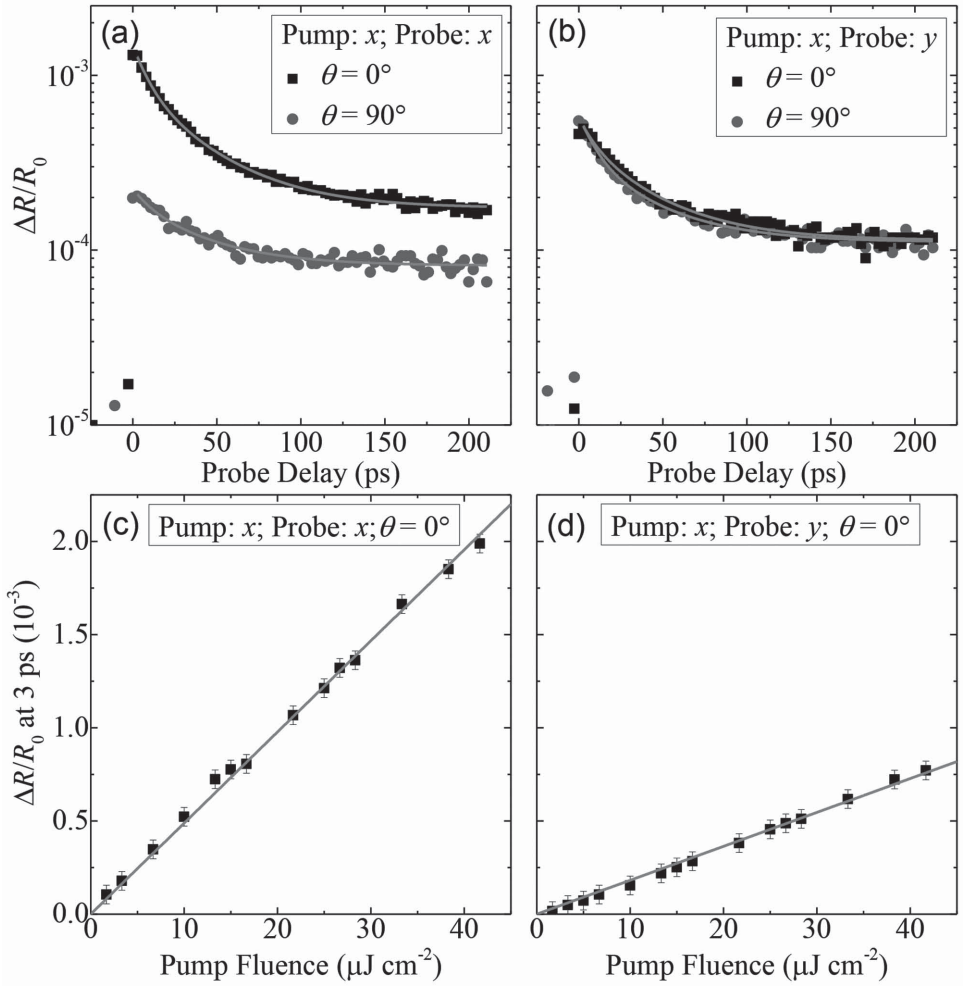

Figure 2. a) Differential reflection signal as a function of the probe delay measured with both pump and probe pulses being polarized along x, and with the angle θ being 0° (squares) and 90° (circles), respectively. The red lines are biexponential functions with two time constants of 10 and 40 ps. b) Same as a) except a y-polarized probe is used. c) Magnitude of the differential reflection signal (represented by the signal measured with a probe delay of 3 ps) as a function of the pump pulse fluence. The pump and probe pulses are both x-polarized and $\theta = 0°$. The red line is a linear fit. d) Same as c) except a y-polarized probe is used.

© 2015 Wiley-VCH Verlag GmbH & Co. KGaA, Weinheim

From these measurements, we conclude that the exciton dynamics observed is independent of the probe polarization and sample orientation. Upon injection, the hot carriers relax their energy and form excitons. In this process, even without carrier and exciton recombination, the differential reflection signal is expected to decrease since free carriers are more efficient than excitons in changing the absorption coefficient at the exciton resonance. Based on this argument, we assign the short time constant of 10 ps to energy relaxation of hot carriers and exciton formation. The long time constant of 40 ps can then be assigned to the lifetime of excitons. Given the extremely low photoluminescence yield of monolayer ReS_2, such a short lifetime is limited by nonradiative recombination of excitons.

4. Anisotropic Transient Absorption Response

Figure 2 clearly shows that the magnitude of the differential reflection signal depends on the crystalline orientation and pump–probe polarizations. To systematically study the anisotropic properties of the differential reflection signal, we repeated these measurements as we varied the angle θ. In these measurements, the pump fluence was kept at 25 μJ cm^{-2}. **Figure 3** shows the signal with a probe delay of 3 ps as a function of θ for x–x (black squares) and x–y (blue circles) pump–probe polarizations, respectively. A rather large anisotropy was observed in the x–x configuration, where the data can be fit with $A\cos 2\theta + B$ with $A = 1.0 \times 10^{-3}$ and $B = 0.63 \times 10^{-4}$. The variation of the data in x–y configuration is smaller.

The angular dependence of the differential reflection can be induced by anisotropic interactions of the sample with both the pump and the probe. To consider the effect of pump, we compare the differential reflection at $\theta = 0°$ of x–x and $\theta = 90°$ of x–y configurations, as shown as the purple double arrow in Figure 3. In both cases, the probe polarization is parallel to the direction indicated by the red arrow in Figure 1a. The only difference is that the pump polarization is parallel (x–x, $\theta = 0°$) or perpendicular (x–y, $\theta = 90°$) to that direction. From the two signal values of 1.06×10^{-3} and 0.42×10^{-3}, we conclude that the pump polarized along the direction indicated by the red arrow in Figure 1a injects a factor of 2.5 higher carrier density that the pump polarized perpendicular to that direction. That indicates that the absorption coefficient of the sample is anisotropic by that factor, with the maximal absorption occurring when the polarization is along that direction. Early studies have shown that in bulk ReS_2, the absorption coefficient is maximal when the polarization is along the **b** direction.[34] Based on this, we can assign the sample direction indicated by the red arrow in Figure 1a as the **b** direction, that is, the direction of the Re atomic chains.

To understand the anisotropic effects of the probe, we compare the results of x–x and x–y configurations both at $\theta = 0°$, as shown as the orange double arrow in Figure 3. In this case, the pump polarizations are both parallel to **b**. Hence they inject the same (and maximal) carrier density. With the signal values of 1.06×10^{-3} (x-probe) and 0.38×10^{-3} (y-probe), we conclude that the probe polarized along **b** is a factor of 2.8 more efficient in sensing carriers and excitons than that polarized perpendicular to **b**. That is, the same exciton density induces a maximal change in absorption coefficient when the probe is polarized along **b**. We note that the anisotropic effects of pump and probe have similar magnitudes (2.8 and 2.5, respectively), which is reasonable since they both originate from the interband transition matrix element. The fact that the pump and probe effects both peak along **b** with similar magnitudes of anisotropy suggests that the variation of signal in x–y configuration should be smaller than x–x, as observed in Figure 3. Finally, the magnitudes of anisotropic effects of pump and probe suggest that in the x–x configuration, the signal at $\theta = 0°$ (where both effects are maximal) should be a factor of 7 larger than $\theta = 90°$ (where both effects are minimal). This is reasonably consistent with the results shown in Figures 2a and 3.

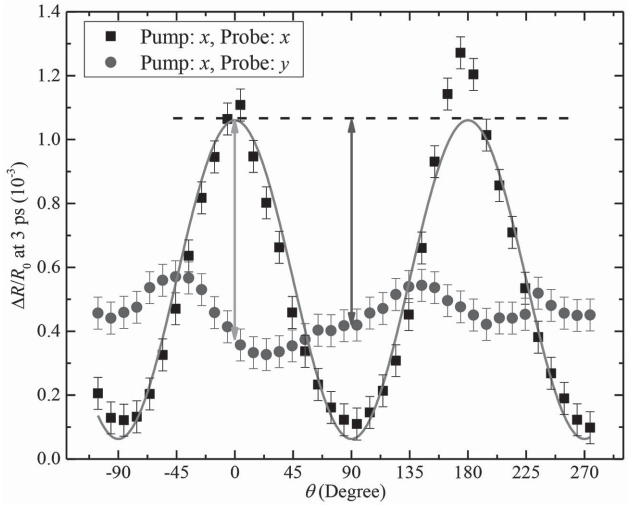

Figure 3. Differential reflection signals at a probe delay of 3 ps measured with pump–probe polarizations of x–x (squares) and x–y (circles). The angle θ is defined in Figure 1a). The red solid line is a fit.

5. Anisotropic Exciton Transport

Having identified the direction of **b**, we next discuss the anisotropic exciton transport property in monolayer ReS_2 by comparing the diffusion coefficients of excitons when they move parallel and perpendicular to the direction of the Re atomic chains. The diffusion coefficient of excitons can be measured by time resolving the evolution of the exciton density profile. According to the diffusion model, with the initial density profile being a Gaussian function, the density profile remains Gaussian and expands due to diffusion.[38] Quantitatively, the area of the profile increases linearly, with the rate determined by the diffusion coefficient, $\sigma^2(t) = \sigma^2(0) + 4Dt$, where D and $\sigma(0)$ are the diffusion coefficient and the $1/e$ half width of the initial spatial profile at $t = 0$.[38]

To measure the diffusion coefficient along the **b** direction, we rotated the sample so that **b** is along x ($\theta = 0°$), and

© 2015 Wiley-VCH Verlag GmbH & Co. KGaA, Weinheim

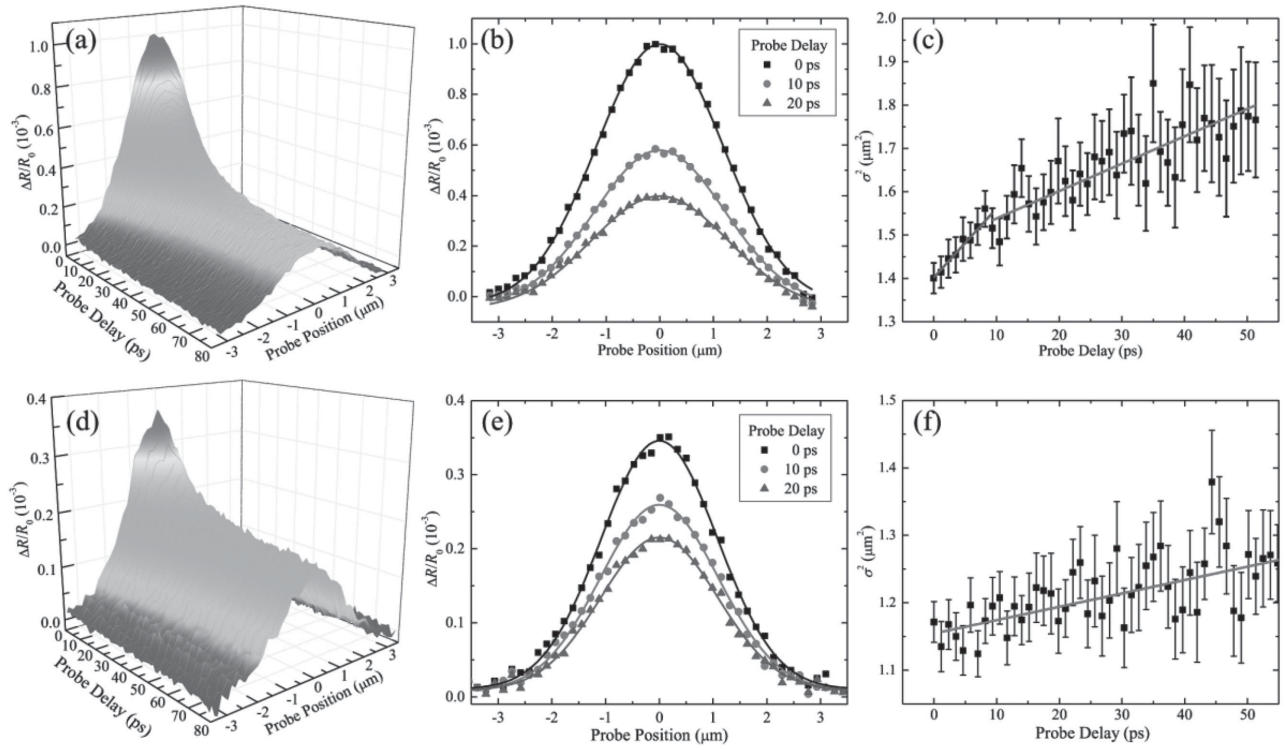

Figure 4. a) Differential reflection signal as a function of probe delay and probe position, as the probe spot is scanned along the **b** direction. The pump and probe polarizations are also along **b**. b) Spatial profiles of the differential reflections signal at probe delays of 0 (squares), 10 (circles), and 20 ps (triangles). The solid lines are Gaussian fits. c) Squared width of the profiles as a function of probe delay. The lines are linear fits for the time ranges of 0 to 10 ps and 10 to 50 ps, respectively. Panels d–f) are the same as a–c), but with the probe spot scan direction and probe polarization being perpendicular to **b**.

measured the differential reflection signal as a function of probe delay as we scan the probe spot along x. The pump and probe were both polarized along x, too, with a pump fluence of 36 μJ cm^{-2}. The result of this spatiotemporal scan is shown in **Figure 4**a. At each probe delay, the profile is a Gaussian function. A few examples of the profiles are shown in Figure 4b, with probe delays of 0 (black squares), 10 (red circles), and 20 ps (blue triangles), respectively. By fitting each profile with a Gaussian function, we deduced its 1/e width. The squared width is plotted as a function of probe delay in Figure 4c. Despite the rather large uncertainties, an expansion of the profile is clearly seen. By fitting the data in the range of 10–50 ps (the red solid line), we obtained a diffusion coefficient of 16 ± 4 cm^2 s^{-1}.

Next, we studied diffusion of excitons along the direction perpendicular to **b** by rotating the sample by 90° so that **b** is along y direction. The pump polarization was also changed to y in order to inject the same carrier density. We repeated the measurements described above under otherwise same conditions. The results are plotted in panels (d), (e), and (f) of Figure 4 in a similar fashion as (a), (b), and (c). We found that the diffusion coefficient along this direction is 5 ± 2 cm^2 s^{-1}, about a factor of 3 smaller than along the **b** direction.

Based on the diffusion coefficients obtained from these measurements, we can deduce the corresponding exciton mobilities, μ, from the Einstein relation $D = \mu k_B T/e$, where k_B, T, and e are Boltzmann constant, the temperature, and elementary charge, respectively. We found the mobilities of about 620 cm^2 V^{-1} s^{-1} along **b** and about 200 cm^2 V^{-1} s^{-1} perpendicular to **b**, respectively. Furthermore, we deduced the exciton diffusion lengths ($L = \sqrt{D\tau}$) of about 250 nm along **b** and about 80 nm when moving perpendicular to **b**, by using the measured exciton lifetime of τ = 40 ps. Similar to the lifetime, this diffusion length is limited by fast nonradiative recombination of excitons. Nevertheless, these values are similar to other TMD monolayers, such as WSe_2 (160 nm),[39] $MoSe_2$ (400 nm),[40] and WS_2 (350 nm).[41]

Finally, Figure 4c shows that in the duration before 10 ps, the slope appears to be larger. A linear fit in this range (the blue solid line) results in a diffusion coefficient of 40 ± 10 cm^2 s^{-1}. This fast diffusion in early delays could be attributed to the hot exciton effect. Initially, the electron–hole pairs are injected with a large excess energy, which then form excitons with a temperature higher than the lattice temperature. As indicated by the Einstein relation, these excitons with higher thermal energy have larger diffusion coefficient, since the mobility is determined by the lattice temperature, and is insensitive to the exciton temperature. We note that this time range is consistent with the short time constant of 10 ps deduced from Figure 2, which was attributed to the exciton formation and energy relaxation. Our interpretations of these two observations are consistent. We note that the low signal-to-noise ratio in Figure 4f does not allow identification of such a regime along the direction perpendicular to **b**.

© 2015 Wiley-VCH Verlag GmbH & Co. KGaA, Weinheim

6. Conclusion

We showed that monolayer ReS_2 possesses in-plane anisotropic optical and transport properties. The absorption coefficient is maximal for light polarized along the **b** lattice vector direction, which is the direction of the Re atomic chains, and decreases by about a factor of 2.5 when the polarization is perpendicular to **b**. The differential reflection signal induced by excitons of a certain density also reaches a maximum when the probe polarization is along **b**, which reduced by a similar factor when the probe polarization is perpendicular to **b**. From time-resolved measurements, we extracted an exciton formation and relaxation time of 10 ps and an exciton lifetime of 40 ps. By resolving the spatiotemporal dynamics of the excitons, we found that the diffusion coefficient of excitons moving along **b** is about 16 $cm^2\ s^{-1}$, which is about a factor of three larger than along the direction perpendicular to **b**. These findings establish monolayer ReS^2 as an anisotropic 2D transition metal dichalcogenide.

7. Experimental Section

The ReS_2 monolayer sample was obtained by polydimethylsiloxane (PDMS)-assisted mechanical exfoliation. A thin film of ReS_2 was first peeled off by a scotch tape. After exfoliation of several times, it was transferred to the surface of PDMS. A flake containing a large and uniform monolayer region was identified, and then transferred to a Si substrate with a 90 nm oxide layer. The thickness of the sample was determined by atomic force microscope (Figure S1, Supporting Information).

In the transient absorption setup, the 532 nm output of a diode laser was used to pump a Ti:sapphire laser, which generates 100 fs pulses with a central wavelength of 810 nm. A beamsplitter was used to pick off 8% of this pulse, which was used as the probe. The majority of the 810 nm pulse was used to pump an optical parametric oscillator, which generates a signal output with a central wavelength of 1460 nm. By focusing the 1460 nm pulse to a beta barium borate crystal, we generated its second harmonic at 730 nm, which was used as the pump. Each pulse goes through a half-wave plate and a polarizer to control its polarization and power. Two dichroic beamsplitters were used to combine the two pulses, which were both focused to the sample by a microscope objective lens. The reflected probe pulse from the sample was sent to a silicon photodetector, output of which was measured by a lock-in amplifier. The pump pulse was modulated by a mechanical chopper at about 2 KHz to improve the signal-to-noise ratio. The sample was fixed on a rotation stage, which was installed on a translation stage. With assist of an imaging system, the laser spots were located at the central region of the monolayer flake, and overlap with the rotation center.

Supporting Information

Supporting Information is available from the Wiley Online Library or from the author.

Acknowledgements

This material is based upon work supported by the National Science Foundation of USA (DMR-0954486, IIA-1430493, and IIA-1430519), National Basic Research Program 973 of China (2011CB932700), Chinese Natural Science Fund Project (61335006, 61378073), Beijing Science and Technology Committee (Z151100003315006), and Swedish Agency for Innovation Systems (2014-04712). The figure captions were updated on November 4, 2015.

[1] K. F. Mak, C. Lee, J. Hone, J. Shan, T. F. Heinz, *Phys. Rev. Lett.* **2010**, *105*, 136805.
[2] A. Splendiani, L. Sun, Y. Zhang, T. Li, J. Kim, C. Y. Chim, G. Galli, F. Wang, *Nano Lett.* **2010**, *10*, 1271.
[3] D. Xiao, G. B. Liu, W. Feng, X. Xu, W. Yao, *Phys. Rev. Lett.* **2012**, *108*, 196802.
[4] H. Zeng, J. Dai, W. Yao, D. Xiao, X. Cui, *Nat. Nanotechnol.* **2012**, *7*, 490.
[5] K. F. Mak, K. He, J. Shan, T. F. Heinz, *Nat. Nanotechnol.* **2012**, *7*, 494.
[6] K. F. Mak, K. He, C. Lee, G. H. Lee, J. Hone, T. F. Heinz, J. Shan, *Nat. Mater.* **2013**, *12*, 207.
[7] J. S. Ross, S. Wu, H. Yu, N. J. Ghimire, A. M. Jones, G. Aivazian, J. Yan, D. G. Mandrus, D. Xiao, W. Yao, X. Xu, *Nat. Commun.* **2013**, *4*, 1474.
[8] A. Chernikov, T. C. Berkelbach, H. M. Hill, A. Rigosi, Y. L. Li, O. B. Aslan, D. R. Reichman, M. S. Hybertsen, T. F. Heinz, *Phys. Rev. Lett.* **2014**, *113*, 076802.
[9] K. He, N. Kumar, L. Zhao, Z. Wang, K. F. Mak, H. Zhao, J. Shan, *Phys. Rev. Lett.* **2014**, *113*, 026803.
[10] H. Zeng, G.-B. Liu, J. Dai, Y. Yan, B. Zhu, R. He, L. Xie, S. Xu, X. Chen, W. Yao, X. Cui, *Sci. Rep.* **2013**, *3*, 1608.
[11] N. Kumar, S. Najmaei, Q. Cui, F. Ceballos, P. M. Ajayan, J. Lou, H. Zhao, *Phys. Rev. B* **2013**, *87*, 161403.
[12] L. M. Malard, T. V. Alencar, A. P. M. Barboza, K. F. Mak, A. M. de Paula, *Phys. Rev. B* **2013**, *87*, 201401.
[13] Y. Li, Y. Rao, K. F. Mak, Y. You, S. Wang, C. R. Dean, T. F. Heinz, *Nano Lett.* **2013**, *13*, 3329.
[14] X. Yin, Z. Ye, D. A. Chenet, Y. Ye, K. O'Brien, J. C. Hone, X. Zhang, *Science* **2014**, *344*, 488.
[15] B. Radisavljevic, A. Radenovic, J. Brivio, V. Giacometti, A. Kis, *Nat. Nanotechnol.* **2011**, *6*, 147.
[16] B. Radisavljevic, M. B. Whitwick, A. Kis, *ACS Nano* **2011**, *5*, 9934.
[17] S. Wi, H. Kim, M. Chen, H. Nam, L. J. Guo, E. Meyhofer, X. Liang, *ACS Nano* **2014**, *8*, 5270.
[18] A. Pospischil, M. M. Furchi, T. Mueller, *Nat. Nanotechnol.* **2014**, *9*, 257.
[19] B. W. H. Baugher, H. O. H. Churchill, Y. Yang, P. Jarillo-Herrero, *Nat. Nanotechnol.* **2014**, *9*, 262.
[20] S. H. Yu, Y. Lee, S. K. Jang, J. Kang, J. Jeon, C. Lee, J. Y. Lee, H. Kim, E. Hwang, S. Lee, J. H. Cho, *ACS Nano* **2014**, *8*, 8285.
[21] A. K. Geim, I. V. Grigorieva, *Nature* **2013**, *499*, 419.
[22] L. Britnell, R. M. Ribeiro, A. Eckmann, R. Jalil, B. D. Belle, A. Mishchenko, Y.-J. Kim, R. V. Gorbachev, T. Georgiou, S. V. Morozov, A. N. Grigorenko, A. K. Geim, C. Casiraghi, A. H. C. Neto, K. S. Novoselov, *Science* **2013**, *340*, 1311.
[23] L. Britnell, R. V. Gorbachev, R. Jalil, B. D. Belle, F. Schedin, A. Mishchenko, T. Georgiou, M. I. Katsnelson, L. Eaves, S. V. Morozov, N. M. R. Peres, J. Leist, A. K. Geim, K. S. Novoselov, L. A. Ponomarenko, *Science* **2012**, *335*, 947.
[24] K. Friemelt, L. Kulikova, L. Kulyuk, A. Siminel, E. Arushanov, C. Kloc, E. Bucher, *J. Appl. Phys.* **1996**, *79*, 9268.

© 2015 Wiley-VCH Verlag GmbH & Co. KGaA, Weinheim

[25] C. H. Ho, P. C. Liao, Y. S. Huang, K. K. Tiong, *Phys. Rev. B* **1997**, *55*, 15608.
[26] C. H. Ho, P. C. Liao, Y. S. Huang, K. K. Tiong, *Solid State Commun.* **1997**, *103*, 19.
[27] C. H. Ho, Y. S. Huang, J. L. Chen, T. E. Dann, K. K. Tiong, *Phys. Rev. B* **1999**, *60*, 15766.
[28] K. Friemelt, M. C. Luxsteiner, E. Bucher, *J. Appl. Phys.* **1993**, *74*, 5266.
[29] G. Leicht, H. Berger, F. Levy, *Solid State Commun.* **1987**, *61*, 531.
[30] S. Tongay, H. Sahin, C. Ko, A. Luce, W. Fan, K. Liu, J. Zhou, Y. S. Huang, C. H. Ho, J. Yan, D. F. Ogletree, S. Aloni, J. Ji, S. Li, J. Li, F. M. Peeters, J. Wu, *Nat. Commun.* **2014**, *5*, 3252.
[31] S. P. Kelty, A. F. Ruppert, R. R. Chianelli, J. Ren, M. H. Whangbo, *J. Am. Chem. Soc.* **1994**, *116*, 7857.
[32] H. H. Murray, S. P. Kelty, R. R. Chianelli, C. S. Day, *Inorg. Chem.* **1994**, *33*, 4418.
[33] C. H. Ho, Y. S. Huang, K. K. Tiong, P. C. Liao, *J. Phys. – Condens. Mat.* **1999**, *11*, 5367.
[34] C. H. Ho, Y. S. Huang, K. K. Tiong, P. C. Liao, *Phys. Rev. B* **1998**, *58*, 16130.
[35] S. Horzum, D. Cakir, J. Suh, S. Tongay, Y. S. Huang, C. H. Ho, J. Wu, H. Sahin, F. M. Peeters, *Phys. Rev. B* **2014**, *89*, 155433.
[36] T. Fujita, Y. Ito, Y. Tan, H. Yamaguchi, D. Hojo, A. Hirata, D. Voiry, M. Chhowalla, M. Chen, *Nanoscale* **2014**, *6*, 12458.
[37] L. V. Keldysh, *Phys. Status Solidi A – Appl. Res.* **1997**, *164*, 3.
[38] D. A. Neamen, *Semiconductor Physics and Devices,* McGraw-Hill, Boston **2002**.
[39] Q. Cui, F. Ceballos, N. Kumar, H. Zhao, *ACS Nano* **2014**, *8*, 2970.
[40] N. Kumar, Q. Cui, F. Ceballos, D. He, Y. Wang, H. Zhao, *Nanoscale* **2014**, *6*, 4915.
[41] J. He, D. He, Y. Wang, Q. Cui, F. Ceballos, H. Zhao, *Nanoscale* **2015**, *7*, 9526.

Received: June 11, 2015
Revised: July 19, 2015
Published online: August 28, 2015

© 2015 Wiley-VCH Verlag GmbH & Co. KGaA, Weinheim